ASSESSMENT OF A COMPREHENSIVE AERO-ACOUSTO-ELASTIC SOLVER FOR ROTORS IN BVI CONDITIONS

Massimo Gennaretti, Giovanni Bernardini, Jacopo Serafini
Roma Tre University, Department of Engineering
Roma, Italy

Gianluca Romani
Delft University of Technology, AWEP Department
Delft, The Netherlands

Abstract

The scope of this paper is the validation of the comprehensive aero-acousto-elastic solver developed in the last years at Roma Tre University against the well-known HART II database, which is the outcome of an international EU-US cooperative research project consisting of a wind tunnel experimental campaign for the measurements of loads, blade deflection, wake shape and noise concerning a 4-bladed model rotor in low-speed descent flight conditions. Comparisons with numerical results available in the literature for the same test cases are also presented. The results provided by the Roma Tre solver are in good agreement with respect to experimental data, with a level of accuracy that is in line with the state-of-the-art predictions. The computational cost requested is limited.

1 INTRODUCTION

HART II test campaign[1;2;3] is the best-known experimental campaign on helicopter rotor aerodynamics, aeroelasticity and aeroacoustics, performed at the DNW low-speed wind tunnel by a joint EU-US consortium. It moved from the previous HART-I research project, including PIV measurements of the wake generated by the examined 4-bladed model rotor. On the whole, HART II has made available to research community data covering trim, elastic motion, aerodynamic loads, wake shape and flow velocity in low-speed descent flight. This flight condition is particularly critical for aeroelastic and aeroacoustic simulations due to the strong interaction between rotor blades and wakes (Blade-Vortex Interaction, BVI, which is one of the major causes of noise and vibratory loads produced by the rotor). Three different operating conditions are considered: the baseline case, in which traditional collective and cyclic controls are applied, and two higher-harmonic controlled cases (HHC), concerning minimum noise and minimum vibration conditions.

In the years following the test campaign, several research centers and academies, including those involved in the HART II project, have been using the outcomes of the project for validation of numerical codes for rotor analysis. The available literature includes the assessment of some comprehensive codes for helicopter rotor analysis based on correlation with HART II data,[4;5] as well as reviews regarding applications of computational fluid dynamics methods coupled with computational structural dynamics codes (CFD/CSD) compared with HART II measurements.[6;7] Among the comprehensive codes correlated in the past with HART II data, it is possible to note contributions from the AFDD and NASA team, Onera, DLR and the University of Maryland.[4;5]

The U.S. Army Aeroflightdynamics Directorate (AFDD) and NASA team used CAMRAD II, in which the structural model is described through finite nonlinear beam elements. The aerodynamic model is derived by combining the modified Onera ELDIN theory for unsteady aerodynamics with C81 standard table lookup. A free-wake model with multiple trailers is applied.

The comprehensive code used by Onera includes a structural model based on finite rigid beam elements with lumped elastic properties. The aerodynamic model is based on a lifting line theory which combines 2-D airfoil tables with the Theodorsen unsteady aerodynamic theory. A prescribed helical wake code is used to find trim condition and blade deformations firstly, then a full span free wake model is applied in order to evaluate blade pressure.

German Aerospace Centre (DLR) used the comprehensive code S4, whose structural model consists of a finite element method based on the Houbold-Brooks formulation. A semi-empirical analytic formulation for the airfoil coefficients, based on the Leiss method for unsteady motion, with enhancements suited for BVI problems, is used for modelling aerodynamics. Fuselage effects are introduced by an analytical formulation based on potential flow theory. The Mangler and Squire wake model is used to evaluate perfor-

mance and vibrations, while an extension of the Beddoes prescribed wake with multiple trailers is used for noise evaluation.

The University of Maryland used UMARC comprehensive code for the HART II correlation study. The aeroelastic solver consists of a finite element method based on a second-order, non-linear, isotropic, Euler-Bernoulli beam blade modeling, loosely coupled with a lifting-line aerodynamics tool and a free-wake wake solver.

All these teams evaluated noise radiation through integration of the Ffwocs Williams and Hawkings equation[8] performed by Farassat's formulation 1A[9].

In this paper, predictions provided by the comprehensive code for helicopter rotor aero-acousto-elastic analysis developed at Roma Tre University in the last twenty years are assessed through comparison with HART II data. It is based the harmonic-balance/modal approach[10] for the integration of the aeroelastic equations obtained by coupling a beam-like model for the structural dynamics of slender, nonuniform, twisted blades, undergoing moderate displacement with the aerodynamic loads given by a boundary element method (BEM) for the solution of free-wake potential flows.[11] The Farassat 1A integral formulation is applied for noise radiation.

In the following, first the aerodynamic, aeroelastic and aeroacoustic formulations applied in the developed solver are outlined, and then predictions concerning aeroelastic response, aerodynamic loads and emitted noise are correlated with HART II measurements.

2 AEROELASTIC SOLVER

The aeroelastic simulations are performed through a modal (Galerkin) approach applied to the blade structural dynamics formulation coupled with aerodynamic loads determined through a boundary integral formulation for potential flows.[10] The aeroelastic computational tool developed is able to evaluate blade elastic response, pressure distribution, and hub loads determining, at the same time, trim and pitch control settings for a prescribed flight condition. Figure 1 depicts the logical scheme of the comprehensive aero-acousto-elastic tool, where the aeroelastic solver (with trim included) is enclosed by the red box.

It is worth noting that, for the analysis of the isolated rotor tested in the HART II project, in the absence of fuselage dynamics, the flight condition to be trimmed is identified by advance ratio, shaft angle and values of steady thrust and rolling and pitching moments at the hub.

Since a stationary flight condition is examined, the time integration of the aeroelastic ordinary differential operator derived after application of the Galerkin method is achieved through a harmonic balance approach, which guarantees a very fast convergence rate of the iterative solution for the nonlinear problem.[10]

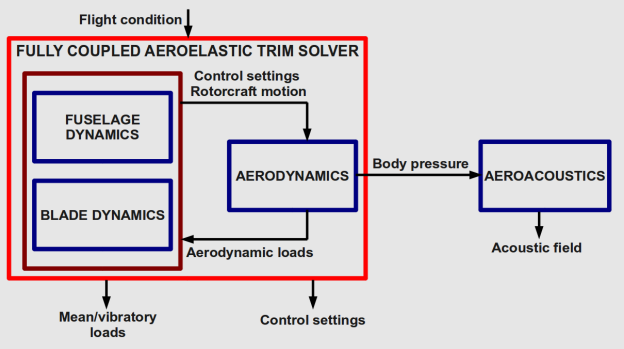

Figure 1: Sketch of the aero-acousto-elastic tool.

2.1 Structural dynamics

Blade structural dynamics is described through a beam-like model. It derives from a nonlinear, bending-torsion formulation valid for slender, homogeneous, isotropic, nonuniform, twisted blades, undergoing moderate displacements.[12] The radial displacement is eliminated from the set of equations by solving it in terms of local tension, and thus the resulting structural operator consists of a set of coupled nonlinear differential equations governing the bending of the elastic axis and the blade torsion.[13] These equations are spatially integrated through the Galerkin approach, with the description of elastic axis deformation and cross-section torsion as linear combinations of shape functions satisfying homogeneous boundary conditions.

This yields a set of nonlinear, ordinary differential equations of the type

$$\boldsymbol{M}\ddot{\boldsymbol{q}}+\boldsymbol{C}\dot{\boldsymbol{q}}+\boldsymbol{K}\boldsymbol{q}=\boldsymbol{f}_{str}^{nl}(t,\boldsymbol{q})+\boldsymbol{f}^{aer}(t,\boldsymbol{q}) \tag{1}$$

where $\boldsymbol{q}$ denotes the vector of the Lagrangian coordinates (time-variant coefficients of the linear combination of shape functions), $\boldsymbol{M}$, $\boldsymbol{C}$, and $\boldsymbol{K}$ are time-periodic mass, damping, and stiffness structural matrices representing the contribution of the linear structural terms. Nonlinear structural contributions are collected in the forcing vector $\boldsymbol{f}_{nl}^{str}$, whereas vector $\boldsymbol{f}^{aer}(t,\boldsymbol{q})$ collects the generalized aerodynamic forces (see Sec. 2.2).

2.2 Aerodynamic formulation

The aerodynamic loads are determined by a BEM approach for the solution of unsteady potential flows around lifting bodies. It is capable of dealing with bodies in arbitrary motion, also in the presence of strong blade-vortex interactions (BVI) occurring in several helicopter flight conditions and sources of annoying noise components.[11;10] It has been successfully applied to aeroacoustic analyses of rotors.[14;15;16;17;18] In the following, the aerodynamic model is briefly outlined.

Considering incompressible, potential flows such that $\boldsymbol{v}=\nabla\varphi$, the aerodynamics formulation applied assumes the potential field, φ, to be given by the superposition of an incident field, φ_I, and a scattered field, φ_S (*i.e.* $\varphi=\varphi_I+\varphi_S$).

The scattered potential is determined by sources and doublets distribution over the surface of the blades, S_B, and by doublets distributed over the wake portion that is very close to the trailing edge from which emanated (near wake, S_W^N). The incident potential field is associated to doublets distributed over the complementary far wake region, S_W^F.[11] The wake surface partition is such that the far wake is the only wake portion that may come in contact with blades and generate BVI effects. The incident potential is discontinuous across S_W^F, whereas the scattered potential is discontinuous across S_W^N and is represented by[11]

$$\begin{aligned}\varphi_S(\boldsymbol{x},t) &= \int_{S_B}\left[G(v_n-u_n)-\varphi_S\frac{\partial G}{\partial n}\right]\mathrm{d}S(\boldsymbol{y}) \\ &- \int_{S_W^N}\Delta\varphi_S\,\frac{\partial G}{\partial n}\,\mathrm{d}S(\boldsymbol{y})\end{aligned} \tag{2}$$

where $G=-1/4\pi r$ is the unit-source solution of the three-dimensional Laplace equation, with $r=\|\boldsymbol{y}-\boldsymbol{x}\|$, while $\Delta\varphi_S$ is the potential jump across the wake surface, known from past history of potential discontinuity at the blade trailing edge through the Kutta-Joukowski condition.[19] In addition, $v_n=\boldsymbol{v}_B\cdot\boldsymbol{n}$, with $\boldsymbol{v}_B$ and $\boldsymbol{n}$ representing blade velocity and outward unit normal, respectively, whereas $u_n=\boldsymbol{u}_I\cdot\boldsymbol{n}$, with $\boldsymbol{u}_I$ denoting the velocity induced by the far wake.

Considering the far wake discretized into M panels, assuming the potential jump to be constant over each panel, and recalling the equivalence between surface distribution of doublets and vortices, the incident velocity field is evaluated through the Biot-Savart law applied to the vortices having the shape of the panel contours. In order to assure a regular distribution of the induced velocity within the vortex core, and thus a stable and regular solution even in BVI conditions, a Rankine finite-thickness vortex model is introduced in the Biot-Savart law.[11] Wake-induced velocity field is applied to evaluate the term u_n in Sec. 2.2, as well as the velocity field from which the wake shape evolution is determined for the free-wake analysis. Note that, for an accurate prediction of BVI phenomena, the accurate evaluation of the wake shape is essential in that a crucial role is played by the relative position between body and wake. The free wake shape is evaluated at the end of each time-step, once the potential solution is known. Figure 2 shows an example of wake shape of the HART II rotor.

In this formulation, the incident potential affects the scattered potential through the induced-velocity, while the scattered potential affects the incident potential by its trailing-edge discontinuity that is convected along the wake and yields the intensity of the vortices of the far wake.[11] Once the potential field is known, the Bernoulli theorem yields the pressure distribution to be provided to aeroelastic and aeroacoustic solvers.[10] The generalized forces $f^{aer}(t,\boldsymbol{q})$ are then evaluated by projection of the sectional loads (suitably modified by the Prandtl-Glauert compressibility correction factor) on the shape functions considered in the Galerkin approach.

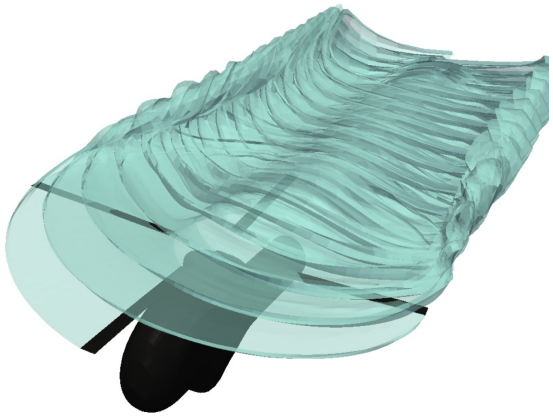

Figure 2: Free-wake shape evaluated for one of the rotor flight conditions (baseline) considered in HART II.

3 AEROACOUSTIC SOLVER

Noise radiated by rotor blades is evaluated through the widely-used boundary integral formulation developed by Farassat[9] for the solution of the Ffowcs Williams and Hawkings equation,[8] which governs propagation of acoustic disturbances aerodynamically generated by moving bodies.

When the velocity of the rotor blades is such that transonic effects are negligible, it yields the aeroacoustic field as a superposition of two terms: the thickness noise, p_T', depending on blade geometry and kinematics,

$$\begin{aligned}4\pi p_T'(\boldsymbol{x},t) &= \int_{S_B}\left[\frac{\rho_0\dot{v}_n}{r|1-M_r|^2}\right]_\tau dS(\boldsymbol{y}) \\ &+ \int_{S_B}\left[\frac{\rho_0 v_n\left(r\dot{M}\cdot\hat{\boldsymbol{r}}+c_0M_r-c_0M^2\right)}{r^2|1-M_r|^3}\right]_\tau dS(\boldsymbol{y})\end{aligned}$$

and the loading noise, p_L', related to the distribution of pressure over blade surfaces,

$$\begin{aligned}4\pi p_L'(\boldsymbol{x},t) &= \frac{1}{c_0}\int_{S_B}\left[\frac{\dot{\tilde{p}}\,\boldsymbol{n}\cdot\hat{\boldsymbol{r}}+\tilde{p}\,\dot{\boldsymbol{n}}\cdot\hat{\boldsymbol{r}}}{r|1-M_r|^2}\right]_\tau dS(\boldsymbol{y}) \\ &+ \int_{S_B}\left[\frac{\tilde{p}\,\boldsymbol{n}\cdot\hat{\boldsymbol{r}}-\tilde{p}\,\boldsymbol{M}\cdot\boldsymbol{n}}{r^2|1-M_r|^2}\right]_\tau dS(\boldsymbol{y}) \\ &+ \frac{1}{c_0}\int_{S_B}\left[\frac{\tilde{p}\,\boldsymbol{n}\cdot\hat{\boldsymbol{r}}}{r^2|1-M_r|^3}r\dot{M}\cdot\hat{\boldsymbol{r}}\right]_\tau dS(\boldsymbol{y}) \\ &+ \int_{S_B}\left[\frac{\tilde{p}\,\boldsymbol{n}\cdot\hat{\boldsymbol{r}}}{r^2|1-M_r|^3}(M_r-M^2)\right]_\tau dS(\boldsymbol{y})\end{aligned}$$

In the above equations, $\boldsymbol{r}$ denotes the distance between observer position, $\boldsymbol{x}$, and source position, $\boldsymbol{y}$, whereas $\hat{\boldsymbol{r}}=\boldsymbol{r}/r$ is the unit vector along the source-observer direction, with $r=|\boldsymbol{r}|$. In addition, c_0 and ρ_0 are speed of sound and density in the undisturbed medium, respectively,

$\tilde{p} = (p - p_0)$ with p_0 representing the undisturbed medium pressure, $\boldsymbol{M} = \boldsymbol{v}_B / c_0$ with $\boldsymbol{v}_B$ denoting the body velocity, $M = \|\boldsymbol{M}\|$, $M_r = \boldsymbol{M} \cdot \hat{\boldsymbol{r}}$, and $v_n = \boldsymbol{v}_B \cdot \boldsymbol{n}$, where $\boldsymbol{n}$ is the outward blade surface unit normal vector. Further, $\dot{v}_n$, $\dot{\boldsymbol{n}}$ and $\dot{\boldsymbol{M}}$ denote time derivatives of v_n, $\boldsymbol{n}$ and $\boldsymbol{M}$, observed in a frame of reference fixed with the undisturbed medium.

The integral contributions are evaluated by a zero-th order boundary element method: the blade surface is divided into quadrilateral panels, and the integrand functions multiplying kernel terms are assumed to be uniformly distributed within each panel, with values equal to those at the centroids. Notation $[...]_\tau$ indicates that these quantities are evaluated at the delayed source time, $\tau = t - \theta$, where θ is the time taken by the signal started from $\boldsymbol{y} \in S_B$ to arrive in $\boldsymbol{x}$ at time t.[9]

In problems dealing with weakly loaded rotors, thickness and loading noise are comparable. However, when strongly loaded rotors are examined (as in the case of BVI occurrence), the thickness noise tends to be negligible and the acoustic disturbance is dominated by the loading noise.

4 NUMERICAL RESULTS

The results of an extensive numerical investigation are presented in order to assess the capability of the outlined aero-acousto-elastic tool to predict the response of rotors subject to BVI phenomena. These are correlated with experimental data concerning the scaled model of the Bo-105 main rotor (radius $R = 2$ m) tested during the HART II program[1;2;3] in the large low-speed facility of the DNW.

The HART II database allows the validation in terms of aeroelastic, aerodynamic and aeroacoustic predictions. Here, the attention is focused on the the baseline case (the minimum-noise and minimum-vibration cases analyzed in HART-II are not considered in this work). The operating condition is a 5.4° descent flight, with advance ratio $\mu = 0.15$ and rotational speed of the rotor $\Omega = 109.12$ rad/sec. A 4985 Nm/rad torsion spring is introduced in order to simulate control chain stiffness effects[4]. Moreover, the complete rotor-fuselage configuration is in aerodynamic and aeroacoustic modeling, while wind tunnel interference effects are neglected.

First, aerodynamic and aeroacoustic analyses are carried out assuming the blade deformations as those measured experimentally[20] (this allows the assessment of the aerodynamic and aeroacoustic prediction capabilities, out of aeroelastic approximation effects). Then, the comprehensive aero-acousto-elastic solver is applied to accomplish the complete solution process starting with rotor and ending with noise radiation. The numerical results carried out in this second approach are compared with those obtained by the University of Maryland (UM) and the German Aerospace Centre (DLR), in order to assess the quality of the present solver with respect to state-of-the-art prediction codes.[4;5] The complete aero-acousto-elastic simulation takes about eight hours on a $i7 - 4770K$ PC.

4.1 Aerodynamic and aeroacoustic analysis for given blade deformation

Aerodynamic and aeroacoustic predictions and correlations are presented in terms of normal force coefficient, tip-vortex trajectories and BVI noise radiation. As already stated, here the blade elastic deformation[20] is assigned as an input to the momentum-trim problem from which blade pitch commands are determined. Table 1 compares the trim settings achieved with those applied experimentally, showing that the discrepancies are quite small ($\leq 5\%$).

	Exp.	Num.	% error
θ_0	3.8°	3.09°	-5.17%
θ_c	1.92°	1.58°	-4.94%
θ_s	-1.34°	-1.46°	2.13%

Table 1: Trim settings from prescribed blade deformation.

Next, Fig. 3 presents the unsteady part (mean value removed) of the $c_n M^2$ coefficient at the spanwise section located at the 87% of the blade span ($r/R = 0.87$). In particular, it compares experimental airloads with those obtained numerically by the present approach. The aerodynamic solver well predicts BVI effects in terms of amplitude and azimuthal location. This is a necessary requisite for the accurate evaluation of noise intensity and directivity, in that these are strongly affected by the position and intensity of BVI phenomena. Some amplitude discrepancies appear in the advancing side, in the interval $[30^\circ, 120^\circ]$.

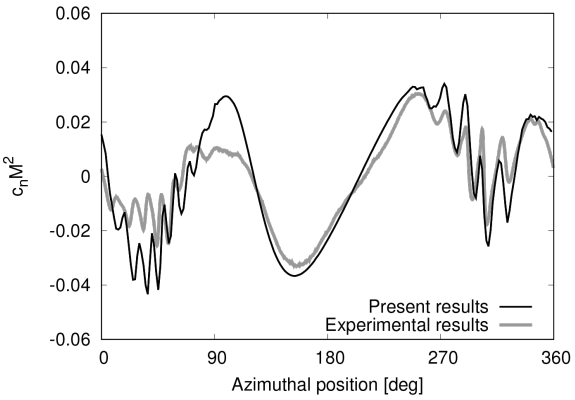

Figure 3: Time history of $c_n M^2$ at $r/R = 0.87$ (mean value removed).

For a deeper investigation on the capability of the prediction tool to capture BVI effects, low-frequency and high-frequency $c_n M^2$ contents are examined separately. Indeed, the low-frequency content (including up to $10/rev$ harmonics) is mainly affected by blade rigid and elastic motion, whereas the high-frequency content strongly depends on wake shape and miss distance. Their correlation with experimental data is provided in Fig. 4. Both numerical results show good agreement with the experimental data, in

particular the high-frequency $c_n M^2$ content underlines the capability of the aerodynamic solver to accurately predict the intensity and the position of high-frequency oscillations due to blade-vortex interactions.

Figure 5 shows the top view of the tip vortices trajectory. The comparison between numerical and experimental results is performed for two different azimuthal positions: $\Psi = 20^\circ$ and $\Psi = 70^\circ$. For both rotor positions a very good agreement between predicted and measured tip vortex trajectories is observed, in both advancing and retreating sides.

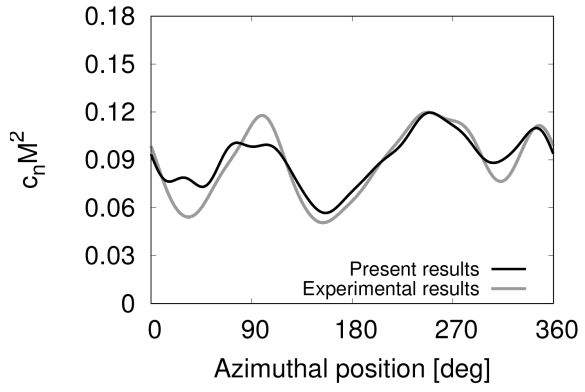

(a) low-frequency (≤ 10/rev)

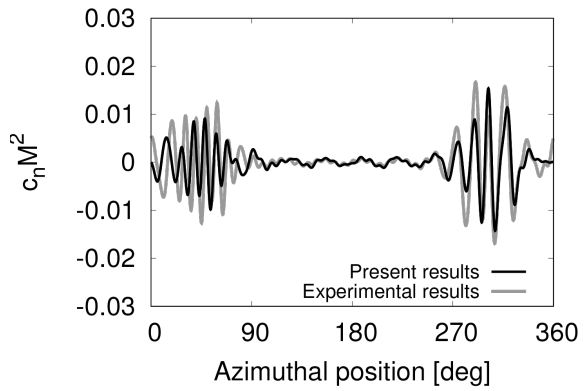

(b) high-frequency (> 10/rev)

Figure 4: Time history of low-frequency and high-frequency contents of $c_n M^2$ at $r/R = 0.87$.

Moreover, Figs. 6(a) and 6(b) show the tip vortex traces on two longitudinal planes. The axial position (z_h coordinate) of the tip vortices is known to have the strongest influence on BVI, because it directly affects the vortex-blade miss distance. The traces are extracted from the intersection of the free-wake shape with the vertical planes at $y_h = 0.7R$ (advancing side) and at $y_h = -0.7R$ (retreating side). Note that, the traces at $x_h > 0$ are identified when one of the rotor blades is at $\Psi = 20^\circ$, whereas the traces at $x_h < 0$ correspond to $\Psi = 70^\circ$. The comparison with the experimental data confirm the very good quality of the wake shape predicted by the aerodynamic solver.

Finally, Fig. 7, shows the comparison between the noise contour map on a horizontal plane placed 2.2 m below the rotor disk computed by the proposed solver and that given by measurements. The contour plots concern the sound pressure level of the mid-frequency noise content including the harmonics between the 6^{th} and the 40^{th} blade-passing frequency (BVISPL). The aeroacoustic predictions are in very good agreement with measurements in terms of both noise level and directivity. These results demonstrate the capability of the aerodynamic-aeroacoustic tool to capture the presence of the two distinct high-noise lobes that are typical of a BVI operating condition, although the extension of that in the retreating side lobe shows some underestimation.

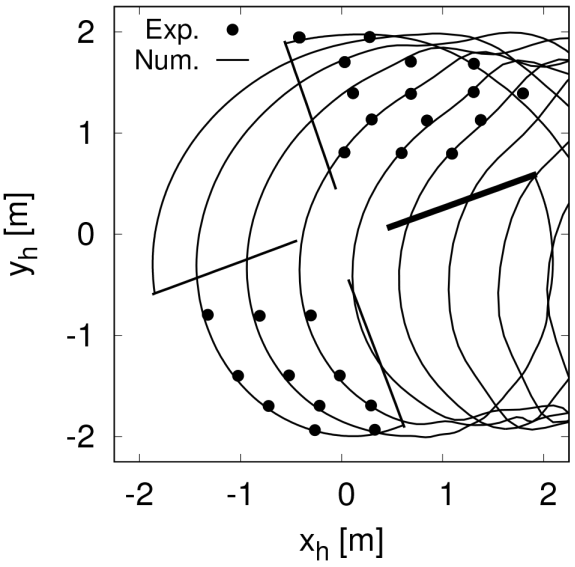

(a) $\Psi = 20^\circ$

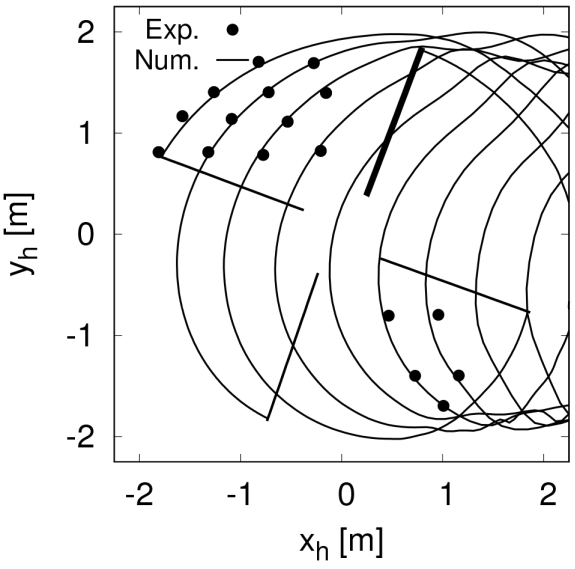

(b) $\Psi = 70^\circ$

Figure 5: Top view of tip vortex trajectories.

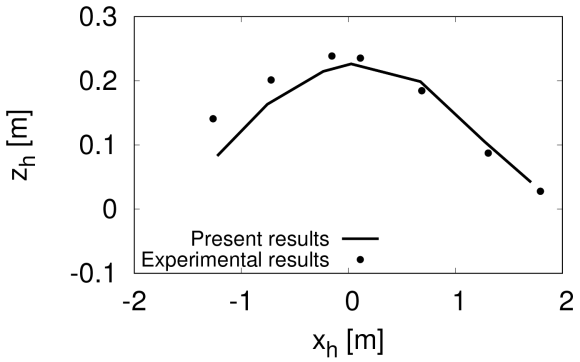

(a) advancing side ($y_h = 0.7R$)

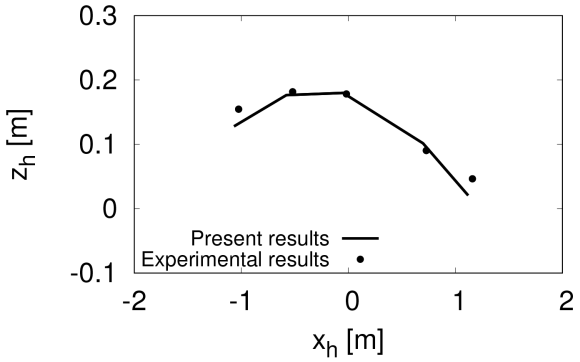

(b) retreating side ($y_h = -0.7R$)

Figure 6: Tip vortex trace on vertical planes.

4.2 Aero-acousto-elastic analysis

Next, the same set of correlations with the experimental data discussed above are presented for the simulations obtained through the complete aero-acousto-elastic comprehensive tool, with inclusion of those concerning the predictions of the blade tip deflections (not considered in the previous analysis).

The corresponding trim setting determined by solving the aeroelastic trim problem are reported in Tab. 2. Compared with those obtained for the blade deformation given by measurements, the agreement with the experimental data is better for collective pitch and lateral cyclic pitch, whereas the longitudinal cyclic pitch presents a larger discrepancy.

	Exp.	Num.	% error
θ_0	3.8°	3.21°	-4.22%
θ_c	1.92°	1.81°	-1.47%
θ_s	-1.34°	-0.77°	-13.45%

Table 2: Trim settings from the complete aeroelastic trim problem.

The corresponding predicted blade deformations are presented in terms of flap, lead-lag and torsion displacements at the blade tip during one rotor revolution in Figs. 8 to 10.

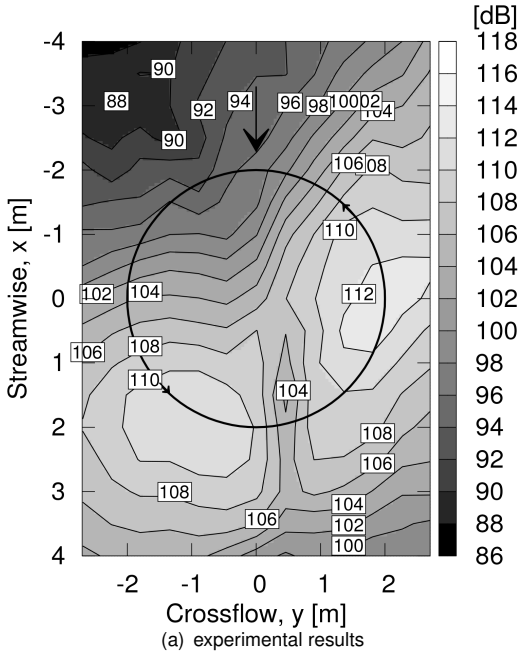

(a) experimental results

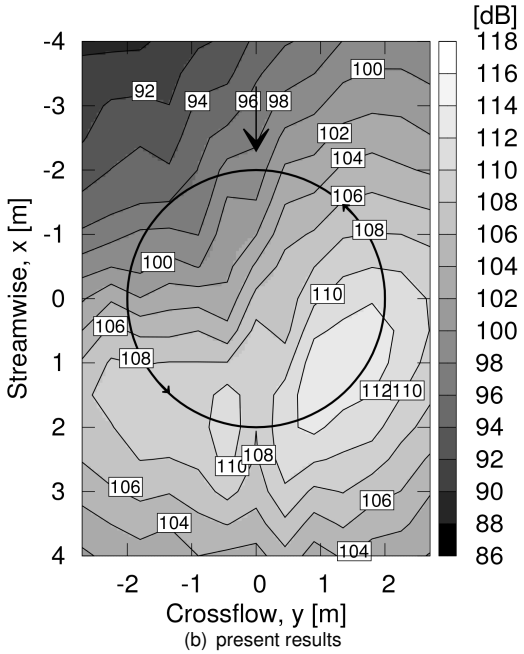

(b) present results

Figure 7: BVISPL contour plots.

Specifically, Fig. 8 shows the comparison of the flapping response with the experimental data and those obtained by UM and DLR.[4;5] The measured deflections show a negative mean value (consistently with the fact that the 3300 N trim thrust is lower than the 3600 N trim thrust design of the pre-cone configuration[5]) and a clear 1/rev variation with maximum upward position at $\Psi = 280^\circ$ and minimum deflection at $\Psi = 100^\circ$. The flap response predicted by the present solver shows a quite accurate behavior, with underestimation of the 1/rev amplitude and a less marked minimum peak around $\Psi = 100^\circ$ (this seems to be related to the discrepancy observed on blade loads in Fig. 3).

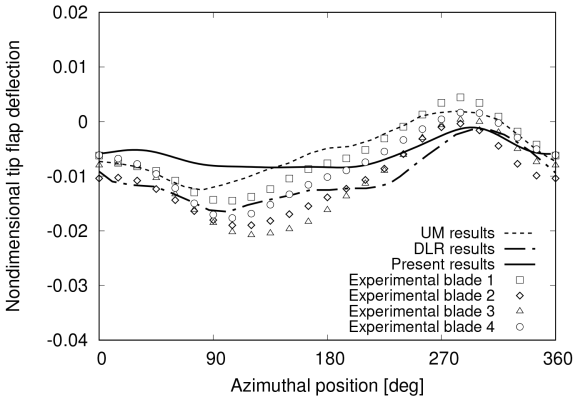

Figure 8: Blade tip flap deflection.

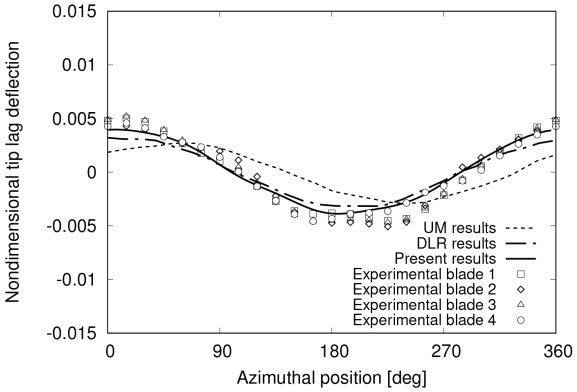

Figure 9: Blade tip lead-lag deflection.

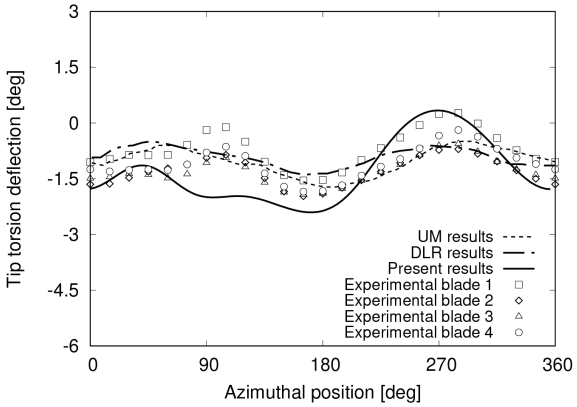

Figure 10: Blade tip torsion deflection.

Then, Fig. 9 depicts the dynamic part of the lead-lag deflection (the mean value has been removed in that affected by a systematic issue.[5]) The present prediction is dominated by the 1/rev component, with maximum forward position reached when the blade is at $\Psi = 180°$, in very good agreement with measured data.

Finally, the blade tip torsion is shown in Fig. 10. The relevant $2/rev$ content that is observed in the experimental data is quite well captured, although some discrepancies appear between $\Psi = 60°$ and $\Psi = 160°$. This is probably related to lack of accuracy of the predicted flap deflection already observed in that azimuth region in Fig. 8.

Given the trim settings of Tab. 2 and the blade deformations of Figs. 8 to 10, the dynamic part of the corresponding predicted $c_n M^2$ coefficient at $r/R = 0.87$ is depicted in Fig. 11, compared with that determined experimentally and provided by UM and DLR computations.[5] Despite some local inaccuracy observed in the evaluated blade deformation, the aeroelastic solver is capable of capturing intensity and location of BVI effects on blade airloads. As it shown in Fig. 12(a), the local inaccuracy of blade deformation affects the low-frequency harmonics of computed airloads which, however, are still satisfactorily predicted. The good quality of the predicted high-frequency airloads is confirmed in Fig. 12(b).

The top view of the tip vortices trajectories given by the comprehensive tool is shown in Figs. 13(a) and 13(b) for the same two azimuthal positions considered in Fig. 5. The correlation with the experimental data is confirmed to be of very good quality, both in the advancing and in the retreating side. In addition, Fig. 14 shows the tip vortex traces on the two longitudinal planes already examined in Fig. 6. Because of the inaccuracy observed in the evaluation of blade deformations, the prediction of the wake shape is slightly less accurate than that provided by the aerodynamic analysis (namely that obtained in Fig. 6 from measured blade deformation). This is especially true in the advancing side, downstream of the rotor hub ($x_h > 0$). Nevertheless, the prediction of the wake geometry remains quite good, if compared with those available from the literature.

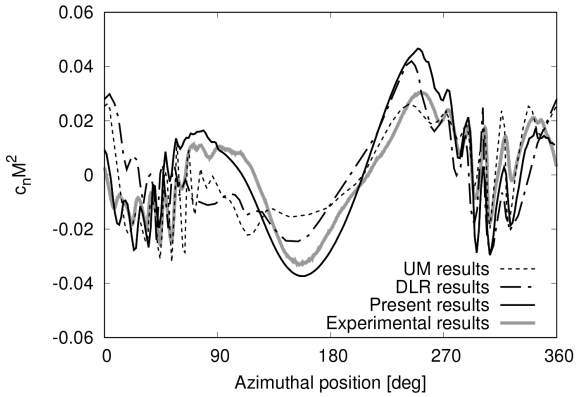

Figure 11: Time history of $c_n M^2$ at $r/R = 0.87$ from aeroelastic solver (mean value removed).

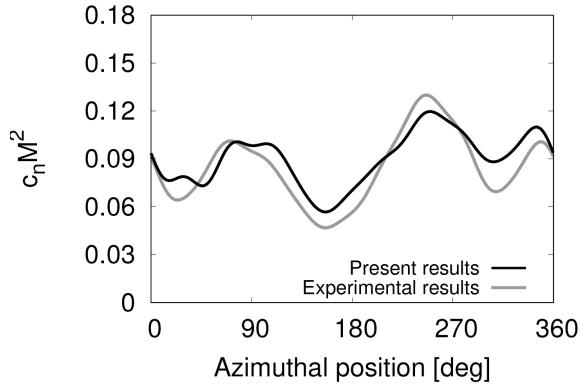

(a) low-frequency (≤ 10/rev)

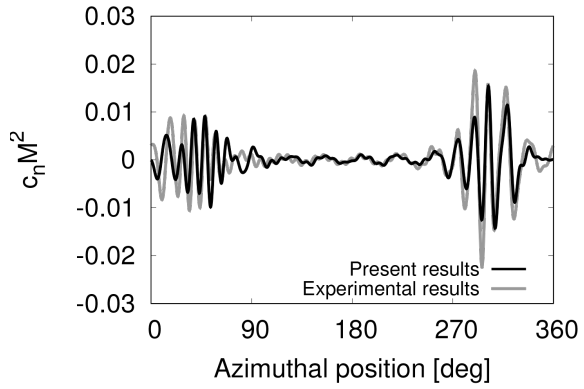

(b) high-frequency (> 10/rev)

Figure 12: Time history of low-frequency and high-frequency contents of c_nM^2 at $r/R = 0.87$ from aeroelastic solver.

Finally, Fig. 15, shows BVISPL contour maps below the rotor disk that are computed starting from the blade surface pressure distribution evaluated through the aeroelastic solver. Compared with the results shown in Fig. 7, it is confirmed that BVI noise directivity and intensity are well predicted, although deriving from the fully numerical process based on the proposed comprehensive solution tool. It is worth noting that, the quality of the correlation between numerical and experimental aeroacoustic data in Fig. 15 is comparable with or even better than that related to the results available in the literature.[4;5]

5 CONCLUSIONS

The comprehensive aero-acousto-elastic code developed in the last years at Roma Tre University has been validated against the well known HART II database. The comparison has been performed over a wide set of results, including trim settings, aerodynamic loads, blade deflections, wake shape and radiated noise. Numerical results available in the literature have been included for comparison. Aerodynamic predictions of wake shape and unsteady airloads, as well as aeroacostic predictions of emitted noise correlate very well with experimental data, and this result is achieved both when the blade deformation is assumed to be that provided by measurements and when it is the result of the aeroelastic solver included in the comprehensive tool. In particular, the solver is capable of capturing intensity and location of aerodynamic load induced by BVI phenomena, along with intensity and directivity of radiated noise. Some inaccuracy is present in the prediction of flap and torsion deflections in the advancing side. In the overall, the results from the proposed code are in good agreement with respect to experimental data, with a level of accuracy that is in line with the state-of-the-art predictions. The computational cost is limited: the complete aero-acousto-elastic simulation is performed in a few hours by a common desktop PC.

ACKNOWLEDGEMENT

The authors gratefully acknowledge the provision of data that was used in this study by the members of the HART II team.

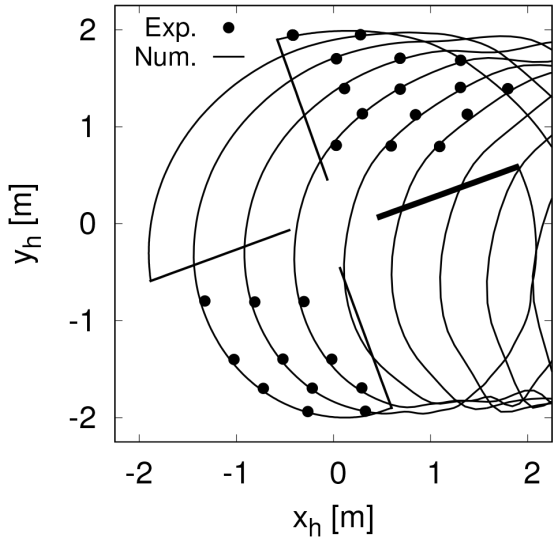

(a) $\Psi = 20^\circ$

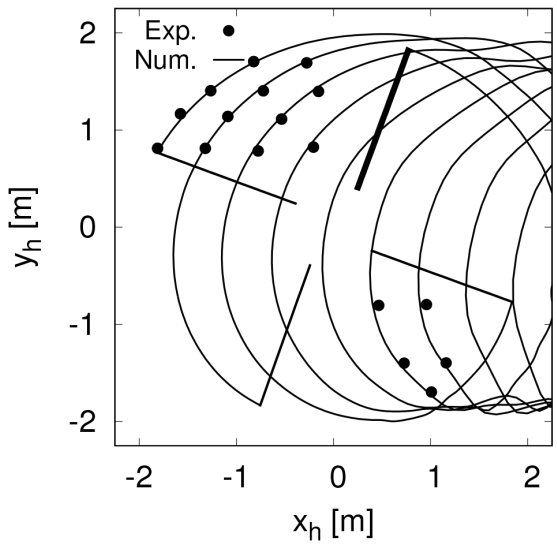

(b) $\Psi = 70^\circ$

Figure 13: Top view of tip vortex trajectories from aeroelastic solver.

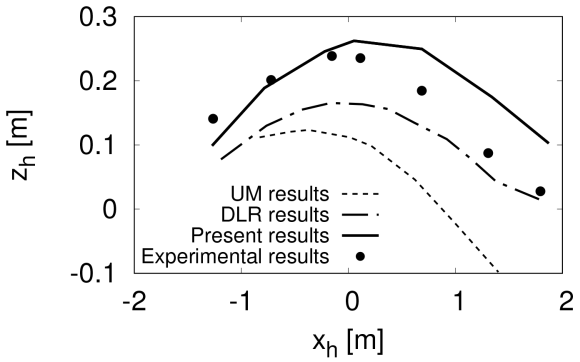

(a) advancing side ($y_h = 0.7R$)

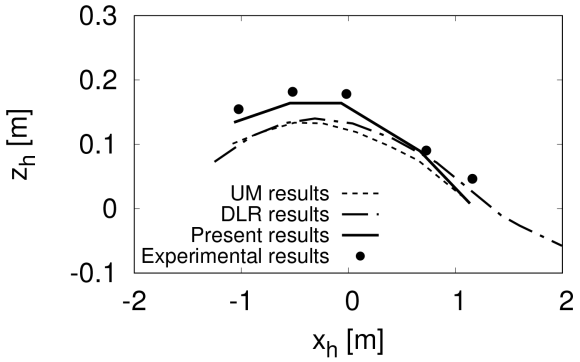

(b) retreating side ($y_h = -0.7R$)

Figure 14: Tip vortex trace on longitudinal planes, baseline.

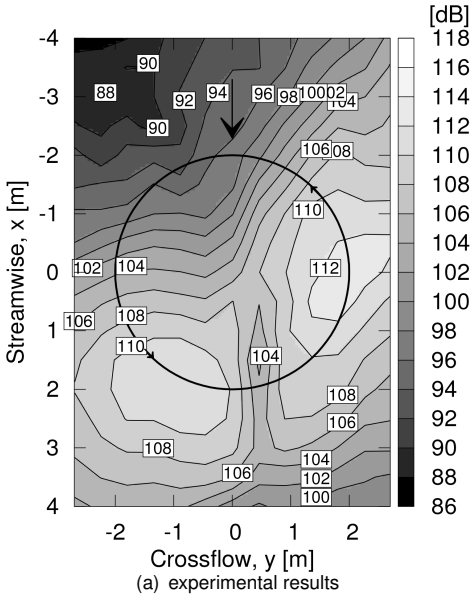

(a) experimental results

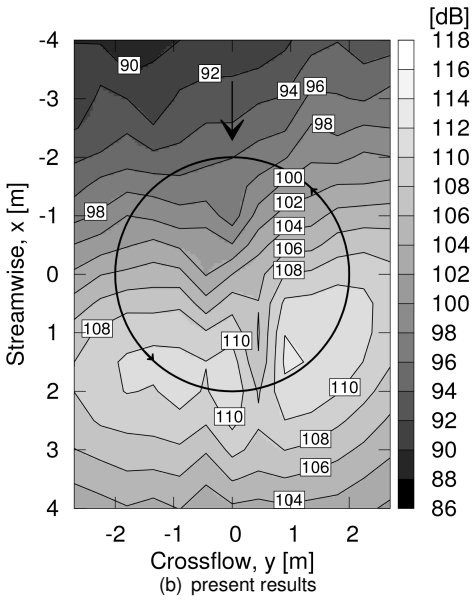

(b) present results

Figure 15: BVISPL contour plots from aero-acousto-elastic solver.

References

[1] B. G. van der Wall, "2nd HHC aeroacoustic rotor test (HART II)-Part I: Test documentation," 2003.

[2] B. G. van der Wall, C. L. Burley, Y. Yu, H. Richard, K. Pengel, and P. Beaumier, "The HART II test–measurement of helicopter rotor wakes," *Aerospace Science and Technology*, vol. 8, no. 4, pp. 273–284, 2004.

[3] B. G. van der Wall and C. L. Burley, "2nd HHC aeroacoustic rotor test (HART II)-part II: representative results," Tech. Rep. IB 111-2005, DLR, 2005.

[4] B. G. van der Wall, J. W. Lim, M. J. Smith, S. N. Jung, J. Bailly, J. D. Baeder, and D. D. Boyd Jr, "An assessment of comprehensive code prediction state-of-the-art using the HART

II international workshop data," in *68th Annual Forum of the American Helicopter Society, Ft. Worth, TX*, 2012.

[5] B. G. van der Wall, J. W. Lim, M. J. Smith, S. N. Jung, J. Bailly, J. D. Baeder, and D. D. Boyd Jr, "The HART II international workshop: an assessment of the state-of-the-art in comprehensive code prediction," *CEAS Aeronautical Journal*, vol. 4, no. 3, pp. 223–252, 2013.

[6] M. J. Smith, J. W. Lim, B. G. van der Wall, J. D. Baeder, R. T. Biedron, D. D. Boyd Jr, B. Jayaraman, S. N. Jung, and B.-Y. Min, "An assessment of CFD/CSD prediction state-of-the-art using the HART II international workshop data," in *68th Annual Forum of the American Helicopter Society, Ft. Worth, TX*, 2012.

[7] M. J. Smith, J. W. Lim, B. G. van der Wall, J. D. Baeder, R. T. Biedron, D. D. Boyd Jr, B. Jayaraman, S. N. Jung, and B.-Y. Min, "The HART II international workshop: an assessment of the state of the art in CFD/CSD prediction," *CEAS Aeronautical Journal*, vol. 4, no. 4, pp. 345–372, 2013.

[8] J. F. Williams and D. L. Hawkings, "Sound generation by turbulence and surfaces in arbitrary motion," *Philosophical Transactions of the Royal Society of London A: Mathematical, Physical and Engineering Sciences*, vol. 264, no. 1151, pp. 321–342, 1969.

[9] F. Farassat, "Derivation of formulations 1 and 1A of Farassat," Tech. Rep. TM-2007-214853, NASA, 2007.

[10] G. Bernardini, J. Serafini, M. Molica Colella, and M. Gennaretti, "Analysis of a structural-aerodynamic fully-coupled formulation for aeroelastic response of rotorcraft," *Aerospace Science and Technology*, vol. 29, no. 1, pp. 175–184, 2013.

[11] M. Gennaretti and G. Bernardini, "Novel boundary integral formulation for blade-vortex interaction aerodynamics of helicopter rotors," *AIAA Journal*, vol. 45, no. 6, pp. 1169–1176, 2007.

[12] D. H. Hodges and E. H. Dowell, "Nonlinear equation for the elastic bending and torsion of twisted nonuniform rotor blades," Tech. Rep. TN D-7818, NASA, 1974.

[13] D. Hodges and R. Ormiston, "Stability of elastic bending and torsion of uniform cantilever rotor blades in hover with variable structural coupling," NASA Technical Note TN D-8192, NASA, 1976.

[14] G. Bernardini, J. Serafini, S. Ianniello, and M. Gennaretti, "Assessment of computational models for the effect of aeroelasticity on bvi noise prediction," *International Journal of Aeroacoustics*, vol. 6, no. 3, pp. 199–222, 2007.

[15] M. Gennaretti, J. Serafini, M. Molica Colella, and G. Bernardini, "Simulation of Helicopter Noise in Maneuvering Flight," in *Proceedings of the 40th European Rotorcraft Forum*, 2014.

[16] G. Bernardini, A. Anobile, J. Serafini, S. Hartjes, and M. Gennaretti, "Methodologies for Helicopter Noise Footprint Prediction in Maneuvering Flights," in *ICSV22*, 2015.

[17] M. Gennaretti, J. Serafini, G. Bernardini, A. Castorrini, G. De Matteis, and G. Avanzini, "Numerical characterization of helicopter noise hemispheres," *Aerospace Science and Technology*, vol. 52, pp. 18–28, 2016.

[18] M. Gennaretti, G. Bernardini, J. Serafini, A. Anobile, and S. Hartjes, "Helicopter noise footprint prediction in unsteady maneuvers," *International Journal of Aeroacoustics*, vol. 16, no. 3, pp. 165–180, 2017.

[19] M. Gennaretti, L. Luceri, and L. Morino, "A unified boundary integral methodology for aerodynamics and aeroacoustics of rotors," *Journal of Sound and Vibration*, vol. 200, no. 4, pp. 467–489, 1997.

[20] B. G. van der Wall, "Mode identification and data synthesis of HART II blade deflection data," Tech. Rep. IB-111-2007/28, DLR, 2007.